

Fundamental limits on the imaging and polarisation properties of far-infrared detectors

Christopher N. Thomas,^{1,*} Stafford Withington,² David T. Chuss,³ Edward J. Wollack,⁴ and S. Harvey Moseley⁵

^{1,2} *Cavendish Laboratory, JJ Thompson Avenue, Cambridge, CB3 0HE, UK*

^{3,4,5} *Observational Cosmology Laboratory, NASA Goddard Space Flight Center, Code 665, Greenbelt, MD, USA*

** Corresponding author: c.thomas@mrao.cam.ac.uk*

Far-infrared bolometric detectors are used extensively in ground-based and space-borne astronomy, and thus it is important to understand their optical behaviour precisely. We have studied the intensity and polarisation response of free-space bolometers, and shown that when the size of the absorber is reduced below a wavelength, the response changes from being that of a classical optical detector to that of a few-mode antenna. We have calculated the modal content of the reception patterns, and found that for any volumetric detector having a side length of less than a wavelength, three magnetic and three electric dipoles characterise the behaviour. The size of the absorber merely determines the relative strengths of the contributions. The same formalism can be applied to thin-film absorbers, where the induced current is forced to flow in a plane. In this case, one magnetic and two electric dipoles characterise the behaviour. The ability to model easily the intensity, polarisation, and straylight characteristics of electrically-small detectors will be of great value when designing high-performance polarimetric imaging arrays.

© 2009 Optical Society of America

OCIS codes: 040.2235, 030.4070, 110.4980, 120.4570

1. Introduction

Focal-plane arrays of far-infrared bolometers are used extensively in ground-based and space-borne astronomy. They can be divided into two categories depending on how power in the

incident radiation field is delivered to the sensing element. In horn or antenna-coupled bolometers, power is collected by a metallic antenna and then delivered to the sensing element through a transmission structure. This transmission structure could be either a single-mode transmission line terminating in a resistive load on the bolometer [1], or a waveguide in which the bolometer is mounted [2]. In free-space coupled bolometers, power is absorbed directly in a bulk material or resistive film [3–5]. The optical behaviour of single-mode horn and antenna-coupled bolometers is well understood. The antenna couples power from the multiple modes of the incoming partially coherent radiation field into the single mode associated with the transmission structure that connects to the antenna. The fully coherent antenna pattern can be referenced through the optical system onto the sky, to give the field distribution to which the complete instrument is sensitive. The equivalent analysis for multimode horns (such as Winston cones) and free-space bolometers is more subtle because the absorber is receptive to power arriving in a number of optical modes simultaneously. In fact, the natural modes of the optical system, the natural modes of the field travelling through the optical system, and the natural modes of the detector are all distinct, and it is more complicated to calculate the precise form of the field distributions to which an instrument responds.

In order to optimize the design of astronomical instruments it is vital to understand the behaviour of free-space bolometers. An optical theory of bolometric detectors has been proposed by Withington [6] and Saklatvala [7]. According to this theory, bolometers are characterised with respect to the field on a reference plane, which is deemed to be the collecting surface of the device. In the case of antenna-coupled bolometers, the collecting surface may be the aperture of a horn, whereas in the case of free-space bolometers, it may be the surface of a resistive film. It is then possible to expand the incident field over this surface in terms of a set of vector basis functions. In the case of partially coherent fields, the expansion coefficients are random variables. For a particular source distribution, however, it is possible to find a set where there is no correlation between the expansion coefficients. We shall refer to the members of this set as the *natural modes* of the incident field. Similarly, it is possible to characterise the response of a bolometer in terms of a set of natural modes, meaning that each mode contributes independently to the recorded output. The total power measured depends on how the natural modes of the field scatter into the natural modes of the detector.

A critical question is how do we determine the optical modes to which a system of absorbing structures is sensitive? The approach often taken at optical wavelengths is to treat a detector as being sensitive to the intensity of the field integrated over the area of the absorber. This approach corresponds to assuming that the response is fully-spatially incoherent and unpolarized over the physical extent of the absorbing surface. To determine the reception

pattern on the sky, a geometrical optics approach is then taken, meaning that the system is assumed to be unpolarized and sensitive to intensity only over the re-imaged outline of the pixel. In this paper we show that this approximation is only valid when the wavelength λ is much smaller than the physical size p of the absorber. This condition is usually satisfied by optical instruments, because the typical size of a CCD pixel is $5 \times 10^{-6}\text{m}$ compared with $5 \times 10^{-7}\text{m}$ for the wavelength of visible light: $p/\lambda \geq 10$. At far-infrared and sub-mm wavelengths, however, devices are being constructed with absorbers that are smaller than the wavelength of operation: $p/\lambda \leq 1$. In order to accommodate this more general case, a full theoretical model of power absorption has been developed [8], which takes into account the state of coherence of the incoming field, and the state of coherence of the physical processes responsible for absorption. The scheme is related to the Method of Moments [9]. Although the approach is rigorous, it is too cumbersome for certain design problems, particularly when one wants to use physical optics to model the behaviour of large-format polarimetric arrays.

In this paper, we adopt an intermediate position, and describe the optical behaviour of free-space bolometers in terms of modes. The underlying principles have already been presented [10,11], but here we extend the analysis considerably. The basic idea is to place a bolometer at the back of an ideal imaging system, which characterises the fact that an incoming field has to travel through free space before arriving at the detector. The degrees of freedom associated with a propagating field are limited, and these restrictions introduce spatial correlations and cross polarisation into the reception pattern. Indeed, as the pixel-size is reduced below a wavelength, the reception pattern becomes increasingly polarized and divergent from its re-imaged geometrical shape. A key part of the work described here is that we explore the state of coherence of the *angular* reception pattern of a naked pixel. In this way, we show that the behaviour of small volumetric detectors, $p/\lambda \leq 1$, can be characterised by three magnetic and three electric dipoles whose relative strengths are determined by the size of the absorber. In the case of thin-film absorbers, where the induced currents are forced to flow in a plane, only one magnetic and two electric dipoles are present.

2. Bolometric detection

The problem of calculating the power absorbed by a free-space bolometer from a field in any state of spatial coherence has been addressed by Withington [6] and Saklatvala [7]. Assume that the incident field is temporally stationary, so that different frequency components, ω , can be treated independently. Let \mathcal{D} be the input reference plane of the detector, and let \mathbf{r}_t be a position vector on this plane. Let $\mathbf{E}_{\mathcal{D}}(\mathbf{r}_t, \omega)$ be the analytic-signal representation of the incident electric field over \mathcal{D} . The first-order spatial correlations can be described by the

space-domain correlation dyadic

$$\bar{\bar{\mathcal{E}}}_{\mathcal{D}}(\mathbf{r}_{t1}, \mathbf{r}_{t2}, \omega) = \langle \mathbf{E}_{\mathcal{D}}(\mathbf{r}_{t1}, \omega) \mathbf{E}_{\mathcal{D}}^*(\mathbf{r}_{t2}, \omega) \rangle, \quad (1)$$

where $\langle \rangle$ denotes the ensemble average. $\bar{\bar{\mathcal{E}}}(\mathbf{r}_{t1}, \mathbf{r}_{t2}, \omega)$ has physical significance beyond the coordinate system used, but a matrix representation can be found by projecting $\bar{\bar{\mathcal{E}}}(\mathbf{r}_{t1}, \mathbf{r}_{t2}, \omega)$ onto a specific basis: $\mathcal{E}_{ij}(\mathbf{r}_{t1}, \mathbf{r}_{t2}, \omega) = \hat{\mathbf{x}}_i(\mathbf{r}_{t1}) \cdot \bar{\bar{\mathcal{E}}}(\mathbf{r}_{t1}, \mathbf{r}_{t2}, \omega) \cdot \hat{\mathbf{x}}_j(\mathbf{r}_{t2})$.

Withington and Saklatvala [6, 7] have shown that the power absorbed by any bolometer can be written in the form

$$\langle p(\omega) \rangle = \int_{\mathcal{D}} d^2\mathbf{r}_{t1} \int_{\mathcal{D}} d^2\mathbf{r}_{t2} \bar{\bar{D}}_{\mathcal{D}}^\dagger(\mathbf{r}_{t1}, \mathbf{r}_{t2}, \omega) \cdot \cdot \bar{\bar{\mathcal{E}}}(\mathbf{r}_{t1}, \mathbf{r}_{t2}, \omega), \quad (2)$$

where the double-dot denotes tensor contraction to a scalar, and \dagger denotes the adjoint. In (2) a new dyadic field, $\bar{\bar{D}}_{\mathcal{D}}(\mathbf{r}_{t1}, \mathbf{r}_{t2}, \omega)$, has been introduced, which characterises the relationship between the state of coherence of the incident field and the output of the detector. We shall refer to it as the *detector response function*.

Both $\bar{\bar{\mathcal{E}}}_{\mathcal{D}}(\mathbf{r}_{t1}, \mathbf{r}_{t2}, \omega)$ and $\bar{\bar{D}}_{\mathcal{D}}(\mathbf{r}_{t1}, \mathbf{r}_{t2}, \omega)$ are Hermitian in all variables, and admit diagonal decompositions:

$$\bar{\bar{\mathcal{E}}}_{\mathcal{D}}(\mathbf{r}_{t1}, \mathbf{r}_{t2}, \omega) = \sum_n \lambda^{(n)} \mathbf{U}^{(n)}(\mathbf{r}_{t1}, \omega) \mathbf{U}^{(n)*}(\mathbf{r}_{t2}, \omega). \quad (3)$$

$\{\lambda^{(n)}\}$ is a set of scalars, and $\{\mathbf{U}^{(n)}(\mathbf{r}_t, \omega)\}$ a set of vector fields. Let $\{\lambda^{(n)}\}$ and $\{\mathbf{U}^{(n)}(\mathbf{r}_t, \omega)\}$ be associated with the decomposition of $\bar{\bar{\mathcal{E}}}_{\mathcal{D}}(\mathbf{r}_{t1}, \mathbf{r}_{t2}, \omega)$, and $\{\gamma^{(m)}\}$ and $\{\mathbf{R}^{(m)}(\mathbf{r}_t, \omega)\}$ with the decomposition of $\bar{\bar{D}}_{\mathcal{D}}(\mathbf{r}_{t1}, \mathbf{r}_{t2}, \omega)$. Substituting these representations into (2) gives

$$\langle p(\omega) \rangle = \sum_{m,n} \gamma^{(m)} \lambda^{(n)} \left| \int_{\mathcal{F}} d^2\mathbf{r}_t \mathbf{R}^{(m)*}(\mathbf{r}_t, \omega) \cdot \mathbf{U}^{(n)}(\mathbf{r}_t, \omega) \right|^2. \quad (4)$$

(3) corresponds to finding the coherent modes of the field [12], with the $\lambda^{(n)}$ corresponding to the fraction of the total power carried by each mode. Each $\mathbf{R}^{(m)}(\mathbf{r}_t, \omega)$ is a fully coherent field to which the detector is sensitive, and each $\gamma^{(m)}$ is the effective responsivity of the mode. In the case of antenna-coupled bolometers, only one $\gamma^{(m)}$ is non-zero, and (4) takes on the well-known form for the power coupled between a coherent field and a radio antenna.

3. Bolometric imaging

Consider an optical system comprising two ideal thin lenses separated by the sum of their focal lengths: Figure 1. A planar bolometer is placed at the focal-plane, \mathcal{F} , of one of the lenses. The system could represent an ideal astronomical telescope, with suitable angular

scaling at the source plane, \mathcal{S} , or a microscope of some kind. The purpose of the model is to bring out fundamental restrictions on the imaging properties of bolometers, aside from constraints due to the optical system. We therefore assume that the lenses are large compared with the wavelength, and that they do not introduce cross-polar scattering. Obviously, the system cannot image the whole field at \mathcal{S} , only the component that is able to propagate to \mathcal{F} .

Assume that the response function of the bolometer at \mathcal{F} is known, $\bar{\bar{D}}_{\mathcal{F}}(\mathbf{r}_{t1}, \mathbf{r}_{t2}, \omega)$, but we would like to characterize the instrument's imaging capabilities at \mathcal{S} . Therefore, it is necessary to relate the response functions at \mathcal{F} and \mathcal{S} . From (2), the power absorbed is

$$\langle p(\omega) \rangle = \int_{\mathcal{F}} d^2\mathbf{r}_{t1} \int_{\mathcal{F}} d^2\mathbf{r}_{t2} \bar{\bar{D}}_{\mathcal{F}}^\dagger(\mathbf{r}_{t1}, \mathbf{r}_{t2}, \omega) \cdot \cdot \bar{\bar{\mathcal{E}}}_{\mathcal{P}}(\mathbf{r}_{t1}, \mathbf{r}_{t2}, \omega), \quad (5)$$

where $\bar{\bar{\mathcal{E}}}_{\mathcal{P}}(\mathbf{r}_{t1}, \mathbf{r}_{t2}, \omega)$ is the coherence tensor of the propagating part, $\mathbf{E}_P(\mathbf{r}_t, \omega)$, of the source-plane field, $\mathbf{E}_S(\mathbf{r}_t, \omega)$. The propagating part can be found by using the angular spectrum of wavefields [13]. If the Fourier transform of $\mathbf{E}_S(\mathbf{r}_t, \omega)$ is

$$\mathbf{A}(\mathbf{k}_t, \omega) = \frac{1}{2\pi} \int_{\mathcal{S}} d^2\mathbf{r}_t \mathbf{E}_S(\mathbf{r}_t, \omega) \exp(-i\mathbf{k}_t \cdot \mathbf{r}_t), \quad (6)$$

then each component is associated with an expansion function of the form $\mathbf{A}(\mathbf{k}_t, \omega) \exp(i\mathbf{k}_t \cdot \mathbf{r}_t) \exp(ik_z(\mathbf{k}_t)z)$, where $\mathbf{k} = \mathbf{k}_t + k_z\hat{\mathbf{z}}$, and $|\mathbf{k}_t|^2 + (k_z(\mathbf{k}_t))^2 = (\omega/c)^2$; it is assumed the source plane is at $z = 0$. Because we are only interested in the part of the field that is able to propagate from \mathcal{S} to \mathcal{F} , we must consider only those Fourier components for which $|\mathbf{k}_t| < (\omega/c)$, and those having vector components transverse to the direction of propagation. We therefore simply discard those Fourier components not associated with plane waves, and invert the transform. Strictly speaking, this approach ignores certain boundary conditions on the tangential component of the E -field at \mathcal{S} , but it is appropriate for our purposes. Applying these constraints gives

$$\mathbf{E}_P(\mathbf{r}_t, \omega) = \frac{1}{2\pi} \int_{|\mathbf{k}_t| < \frac{\omega}{c}} d^2\mathbf{k}_t \left(\bar{\bar{\mathcal{I}}} - \hat{\mathbf{k}}\hat{\mathbf{k}} \right) \cdot \mathbf{A}(\mathbf{k}_t, \omega) \exp(i\mathbf{k}_t \cdot \mathbf{r}_t), \quad (7)$$

where $\bar{\bar{\mathcal{I}}}$ is the unit dyadic in three-dimensions, and $\bar{\bar{\mathcal{I}}} - \hat{\mathbf{k}}\hat{\mathbf{k}}$ strips out any longitudinally polarized component. Using (7), the correlation dyadic of the propagating field becomes

$$\begin{aligned} \bar{\bar{\mathcal{E}}}_{\mathcal{P}}(\mathbf{r}_{t1}, \mathbf{r}_{t2}, \omega) &= \frac{1}{(2\pi)^2} \int_{|\mathbf{k}_{t1}| < \frac{\omega}{c}} d^2\mathbf{k}_{t1} \int_{|\mathbf{k}_{t2}| < \frac{\omega}{c}} d^2\mathbf{k}_{t2} \exp(i\mathbf{k}_{t1} \cdot \mathbf{r}_{t1}) \exp(-i\mathbf{k}_{t2} \cdot \mathbf{r}_{t2}) \\ &\times \left(\bar{\bar{\mathcal{I}}} - \hat{\mathbf{k}}_1\hat{\mathbf{k}}_1 \right) \cdot \bar{\bar{\mathcal{A}}}(\mathbf{k}_{t1}, \mathbf{k}_{t2}, \omega) \cdot \left(\bar{\bar{\mathcal{I}}} - \hat{\mathbf{k}}_2\hat{\mathbf{k}}_2 \right), \end{aligned} \quad (8)$$

where $\bar{\bar{\mathbf{A}}}(\mathbf{k}_{t1}, \mathbf{k}_{t2}, \omega) = \langle \mathbf{A}(\mathbf{k}_{t1}, \omega) \mathbf{A}^*(\mathbf{k}_{t2}, \omega) \rangle$ is the k -domain correlation dyadic.

It is now possible to relate the detector response functions at the focal and source planes. Substituting (8) in (5), and changing the order of integration, gives

$$\langle p(\omega) \rangle = \int_{|\mathbf{k}_t| < \frac{\omega}{c}} d^2 \mathbf{k}_{t1} \int_{|\mathbf{k}_t| < \frac{\omega}{c}} d^2 \mathbf{k}_{t2} \left[\left(\bar{\bar{\mathcal{I}}} - \hat{\mathbf{k}}_1 \hat{\mathbf{k}}_1 \right) \cdot \bar{\bar{\mathcal{G}}}(\mathbf{k}_{t1}, \mathbf{k}_{t2}, \omega) \cdot \left(\bar{\bar{\mathcal{I}}} - \hat{\mathbf{k}}_2 \hat{\mathbf{k}}_2 \right) \right]^\dagger \cdots \bar{\bar{\mathbf{A}}}(\mathbf{k}_{t1}, \mathbf{k}_{t2}, \omega). \quad (9)$$

$\bar{\bar{\mathcal{G}}}(\mathbf{k}_{t1}, \mathbf{k}_{t2}, \omega)$ is the k -domain representation of the detector response function on the focal plane:

$$\bar{\bar{\mathcal{G}}}(\mathbf{k}_{t1}, \mathbf{k}_{t2}, \omega) = \frac{1}{(2\pi)^2} \int_{\mathcal{F}} d^2 \mathbf{r}_{t1} \int_{\mathcal{F}} d^2 \mathbf{r}_{t2} \bar{\bar{D}}_{\mathcal{F}}(\mathbf{r}_{t1}, \mathbf{r}_{t2}, \omega) \exp(-i\mathbf{k}_{t1} \cdot \mathbf{r}_{t1}) \exp(+i\mathbf{k}_{t2} \cdot \mathbf{r}_{t2}). \quad (10)$$

Finally, (9) can be cast back into the space domain giving

$$\langle p(\omega) \rangle = \int_{\mathcal{S}} d^2 \mathbf{r}_{t1} \int_{\mathcal{S}} d^2 \mathbf{r}_{t2} \bar{\bar{D}}_{\mathcal{S}}^\dagger(\mathbf{r}_{t1}, \mathbf{r}_{t2}, \omega) \cdots \bar{\bar{\mathcal{E}}}_{\mathcal{S}}(\mathbf{r}_{t1}, \mathbf{r}_{t2}, \omega), \quad (11)$$

with

$$\begin{aligned} \bar{\bar{D}}_{\mathcal{S}}(\mathbf{r}_{t1}, \mathbf{r}_{t2}, \omega) &= \frac{1}{(2\pi)^2} \int_{|\mathbf{k}_t| < \frac{\omega}{c}} d^2 \mathbf{k}_{t1} \int_{|\mathbf{k}_t| < \frac{\omega}{c}} d^2 \mathbf{k}_{t2} \left(\bar{\bar{\mathcal{I}}} - \hat{\mathbf{k}}_1 \hat{\mathbf{k}}_1 \right) \cdot \bar{\bar{\mathcal{G}}}(\mathbf{k}_{t1}, \mathbf{k}_{t2}, \omega) \cdot \left(\bar{\bar{\mathcal{I}}} - \hat{\mathbf{k}}_2 \hat{\mathbf{k}}_2 \right) \\ &\times \exp(i\mathbf{k}_{t1} \cdot \mathbf{r}_{t1}) \exp(-i\mathbf{k}_{t2} \cdot \mathbf{r}_{t2}). \end{aligned} \quad (12)$$

(10) and (12) together provide a relationship between the response functions at \mathcal{F} and \mathcal{S} . Notice that the state of polarization and spatial-coherence of the detector's response are altered when referenced to \mathcal{S} . The limits on the integrals filter the spatial-frequency components, and introduce coherence into the reception pattern, which affects its modal structure. Although an optical system will, in reality, introduce additional constraints, (12) represents the minimum filtering that a re-referenced response function must incur to give a reception pattern.

In astronomy, sources are incoherent, and the equivalent source-plane field can be written

$$\bar{\bar{\mathcal{E}}}_{\mathcal{S}}(\mathbf{r}_{t1}, \mathbf{r}_{t2}, \omega) = \sum_{i,j=1}^2 E_{ij}(\mathbf{r}_{t1}, \mathbf{r}_{t2}, \omega) \hat{\mathbf{x}}_i \hat{\mathbf{x}}_j \delta(\mathbf{r}_{t1} - \mathbf{r}_{t2}), \quad (13)$$

where $\{\hat{\mathbf{x}}_i\}$ is a set of orthonormal basis vectors lying in the plane. Substituting (13) into

(11) and letting $D_{ij} = \hat{\mathbf{x}}_i \cdot \bar{\mathcal{D}}_S \cdot \hat{\mathbf{x}}_j$, we obtain

$$\langle p(\omega) \rangle = \sum_{i,j=1}^2 \int_S d^2\mathbf{r}_t D_{ij}^*(\mathbf{r}_t, \mathbf{r}_t, \omega) E_{ij}(\mathbf{r}_t, \mathbf{r}_t, \omega). \quad (14)$$

It follows from (1) that the $E_{ij}(\mathbf{r}_t, \mathbf{r}_t, \omega)$ are elements of a 2×2 Hermitian matrix. The matrix can therefore be expanded in Pauli-spin matrices,

$$\left\{ \sigma^{(1)} = \begin{pmatrix} 1 & 0 \\ 0 & 1 \end{pmatrix}, \sigma^{(2)} = \begin{pmatrix} 1 & 0 \\ 0 & -1 \end{pmatrix}, \sigma^{(3)} = \begin{pmatrix} 0 & 1 \\ 1 & 0 \end{pmatrix}, \sigma^{(4)} = \begin{pmatrix} 0 & i \\ -i & 0 \end{pmatrix} \right\}, \quad (15)$$

or

$$E_{ij}(\mathbf{r}_t, \mathbf{r}_t, \omega) = \frac{1}{2} \sum_{k=1}^4 \chi^{(k)}(\mathbf{r}_t, \omega) \sigma_{ij}^{(k)}, \quad (16)$$

where the coefficients are given by

$$\chi^{(k)}(\mathbf{r}_t, \omega) = \sum_{i,j=1}^2 E_{ij}(\mathbf{r}_t, \mathbf{r}_t, \omega) \sigma_{ji}^{(k)}. \quad (17)$$

If we let $\{\hat{\mathbf{x}}_1, \hat{\mathbf{x}}_2\} = \{\hat{\mathbf{x}}, \hat{\mathbf{y}}\}$, then the $\chi^{(k)}$ correspond to the Stokes parameters of the field on the source plane. Substituting (16) into (14), we obtain

$$\langle p(\omega) \rangle = \int_S d^2\mathbf{r}_t \mathcal{R}^*(\mathbf{r}_t, \omega) \cdot \boldsymbol{\chi}(\mathbf{r}_t, \omega), \quad (18)$$

where $\boldsymbol{\chi}$ is the vector of Stokes parameters. The components of $\mathcal{R}(\mathbf{r}_t, \omega)$ are given by

$$\mathcal{R}^{(k)}(\mathbf{r}_t, \omega) = \frac{1}{2} \sum_{i,j=1}^2 D_{ij}(\mathbf{r}_t, \mathbf{r}_t, \omega) \sigma_{ji}^{(k)}, \quad (19)$$

and they are the position-dependent Stoke's parameters of the partially coherent reception pattern of the bolometer. Thus, in the case of spatially incoherent fields, the full response dyadic can be replaced with a position-dependent vector, $\boldsymbol{\chi}(\mathbf{r}_t, \omega)$, which describes the response of the detector to different states of polarisation.

4. Square bolometers

Consider a square bolometer having side length p , and assume that the physical process responsible for energy absorption is uniform, unpolarized and local. The focal-plane response

function is then

$$\bar{\bar{D}}_{\mathcal{F}}(\mathbf{r}_{t1}, \mathbf{r}_{t1}, \omega) = \begin{cases} \alpha \bar{\bar{I}} \delta(\mathbf{r}_{t1} - \mathbf{r}_{t1}) & |x_1|, |x_2|, |y_1|, |y_2| \leq \frac{p}{2} \\ \bar{\bar{0}} & \text{elsewhere} \end{cases}. \quad (20)$$

$\mathbf{r}_t \equiv (x, y)$, and we have assumed that the origin lies at the centre of the absorber. $\bar{\bar{I}}$ and $\bar{\bar{0}}$ are the 3×3 identity and zero dyadics. α is a model parameter representing the absorptivity of the bolometer and is assumed to be a constant. At \mathcal{F} , the natural modes of the bolometer, ignoring edge effects, form a degenerate continuum spanning all possible field states over the region defined by the absorber. An important question is whether this model can represent any physically realizable device. The model was formulated originally to describe black-body absorbers, and so can best be thought of as representing the response of a square aperture in the wall of an integrating cavity. Alternatively, it can be thought of as representing a thick, volumetric absorber, where scattering has, strictly speaking, been ignored. The absorber is volumetric in the sense that it responds to the z -directed component of the incident electric field, or equivalently to current flow in the z direction, as well as in the plane. By considering ohmic power dissipation in the absorber, it is very easy to arrive at (20). This model contrasts with that of a thin film absorber, which will be considered later.

Combining (20), (10) and (12), gives the response function on the sky,

$$\bar{\bar{D}}_{\mathcal{S}}(\mathbf{r}_{t1}, \mathbf{r}_{t1}, \omega) = \frac{1}{(2\pi)^2} \int d^2\mathbf{k}_{t1} \int d^2\mathbf{k}_{t2} \bar{\bar{M}}(\mathbf{k}_{t1}, \mathbf{k}_{t2}, \omega) \exp(-i\mathbf{k}_{t1} \cdot \mathbf{r}_{t1}) \exp(+i\mathbf{k}_{t2} \cdot \mathbf{r}_{t2}), \quad (21)$$

where

$$\begin{aligned} \bar{\bar{M}}(\mathbf{k}_{t1}, \mathbf{k}_{t2}, \omega) &= H\left(\frac{\omega}{c} - |\mathbf{k}_{t1}|\right) H\left(\frac{\omega}{c} - |\mathbf{k}_{t2}|\right) \\ &\times \alpha \left(\bar{\bar{I}} - \hat{\mathbf{k}}_1 \hat{\mathbf{k}}_1\right) \cdot \left(\bar{\bar{I}} - \hat{\mathbf{k}}_2 \hat{\mathbf{k}}_2\right) \\ &\times \mathcal{S}(\mathbf{k}_{t1}, \mathbf{k}_{t2}, \omega), \end{aligned} \quad (22)$$

and H is the Heaviside step function. The two Heaviside terms represent the necessary restriction on $|\mathbf{k}_t|$ for k_z to be real and positive. The dyadic operators in (22) strip out any longitudinal field component, and introduce coupling between the polarisation states of the wave-fields. We shall refer to $\mathcal{S}(\mathbf{k}_{t1}, \mathbf{k}_{t2}, \omega)$ as the *shape function* because it encodes all information about the shape of the pixel. It is given by

$$\mathcal{S}(\mathbf{k}_{t1}, \mathbf{k}_{t2}, \omega) = \frac{1}{(2\pi)^2} \int_{\mathcal{A}} d^2\mathbf{r}_t \exp(i(\mathbf{k}_{t1} - \mathbf{k}_{t2}) \cdot \mathbf{r}_t) \quad (23)$$

where \mathcal{A} is the square region occupied by the absorber, $|x|, |y| \leq p/2$. Free-space absorbers having different shapes can be modelled simply by changing \mathcal{A} . In the case where \mathcal{A} is a

square

$$\begin{aligned}
\mathcal{S}(\mathbf{k}_{t1}, \mathbf{k}_{t2}, \omega) &= \frac{1}{(2\pi)^2} \left[\int_{-\frac{p}{2}}^{\frac{p}{2}} dx \exp(i(\mathbf{k}_{t1} - \mathbf{k}_{t2}) \cdot \hat{\mathbf{x}} x) \right] \\
&\times \left[\int_{-\frac{p}{2}}^{\frac{p}{2}} dy \exp(i(\mathbf{k}_{t1} - \mathbf{k}_{t2}) \cdot \hat{\mathbf{y}} y) \right] \\
&= \left(\frac{p}{2\pi} \right)^2 \text{sinc} \left[\frac{p}{2\pi} (\mathbf{k}_{t2} - \mathbf{k}_{t1}) \cdot \hat{\mathbf{x}} \right] \\
&\times \text{sinc} \left[\frac{p}{2\pi} (\mathbf{k}_{t2} - \mathbf{k}_{t1}) \cdot \hat{\mathbf{y}} \right],
\end{aligned} \tag{24}$$

where we have introduced the normalised sinc function $\text{sinc}(x) = \sin(\pi x)/(\pi x)$.

Although (24) has a simple form, there is no obvious analytic solution to (21), and so the transformation must be achieved numerically. There are two possible options: The first is to evaluate the integrals directly. In this case, the symmetries can be exploited, meaning that only the values of the coherence dyadic over an octant of the plane about the pixel centre need to be calculated explicitly. The second, which we will describe here, involves calculating the response function using a superposition of fundamental modes. It will be shown that this latter technique is both numerically advantageous and provides better physical insight, especially in the p/λ limit in which the number of required modes is small.

From (22) and (24) it can be seen that $\bar{\mathcal{M}}(\mathbf{k}_{t1}, \mathbf{k}_{t2}, \omega)$ is Hermitian in all variables, and therefore has a decomposition of the form

$$\bar{\mathcal{M}}(\mathbf{k}_{t1}, \mathbf{k}_{t2}, \omega) = \sum_n \gamma^{(n)} \mathbf{V}^{(n)}(\mathbf{k}_{t1}, \omega) \mathbf{V}^{(n)*}(\mathbf{k}_{t2}, \omega), \tag{25}$$

where the $\gamma^{(n)}$ and $\mathbf{V}^{(n)}(\mathbf{r}_t, \omega)$ are solutions of

$$\int d^2\mathbf{k}_{t2} \bar{\mathcal{M}}(\mathbf{k}_{t1}, \mathbf{k}_{t2}, \omega) \cdot \mathbf{V}^{(n)}(\mathbf{k}_{t2}, \omega) = \gamma^{(n)} \mathbf{V}^{(n)}(\mathbf{k}_{t1}, \omega). \tag{26}$$

The integrals are evaluated over the entire \mathbf{k}_t -plane. The $\mathbf{V}^{(n)}(\mathbf{r}_{t1}, \omega)$ are the natural modes of the detector, as discussed in Section 2, but now in the k -domain, and for fields on the sky. Substituting (25) into (21), gives

$$\bar{\mathcal{D}}_S(\mathbf{r}_{t1}, \mathbf{r}_{t2}, \omega) = \sum_n \gamma^{(n)} \mathbf{U}^{(n)}(\mathbf{r}_t, \omega) \mathbf{U}^{(n)*}(\mathbf{r}_t, \omega). \tag{27}$$

where

$$\mathbf{U}^{(n)}(\mathbf{r}_t, \omega) = \frac{1}{2\pi} \int d^2\mathbf{k}_t \mathbf{V}^{(n)}(\mathbf{k}_t, \omega) \exp(i\mathbf{k}_t \cdot \mathbf{r}_t). \tag{28}$$

It follows from (27) that the $\gamma^{(n)}$ and $\mathbf{U}^{(n)}(\mathbf{r}_t, \omega)$ are solutions of

$$\int_{\mathcal{S}} d^2\mathbf{r}_t \bar{\bar{\mathcal{D}}}_S(\mathbf{r}_{t1}, \mathbf{r}_{t2}, \omega) \cdot \mathbf{U}^{(n)}(\mathbf{r}_{t2}, \omega) = \gamma^{(n)} \mathbf{U}^{(n)}(\mathbf{r}_{t1}, \omega), \quad (29)$$

which are the natural optical modes of the detector's response function on the source plane. This analysis shows that the modes constitute a set of domain-independent fields, and therefore have true physical significance. For our purposes, it provides an efficient alternative to (21) for transforming between $\bar{\mathcal{M}}(\mathbf{k}_{t1}, \mathbf{k}_{t2}, \omega)$ and $\bar{\bar{\mathcal{D}}}_S(\mathbf{r}_{t1}, \mathbf{r}_{t2}, \omega)$. The procedure is as follows: (i) Calculate a sampled version of $\bar{\mathcal{M}}(\mathbf{k}_{t1}, \mathbf{k}_{t2}, \omega)$ using (22); (ii) diagonalise according to (26), (iii) transform the modes into the space domain using (28); and (iv) reconstruct $\bar{\bar{\mathcal{D}}}_S(\mathbf{r}_{t1}, \mathbf{r}_{t2}, \omega)$ using (27).

This modal approach has two distinct advantages over the direct evaluation of the integral in (21). First, though the modal decomposition requires some numerical overhead, understanding the natural modes of the system provides significant physical insight into its optical behaviour, especially in the limit where the pixel is smaller than the wavelength. Second, the modal approach is numerically more efficient. Consider transforming the response function from a grid of points in the Fourier-domain to a grid of points in the space-domain. The number of two-dimensional Fourier transforms that must be performed to evaluate (21) scales with the square of the number of sample points. In the modal case it scales with the number of modes with nonzero eigenvalues. Even when pixel symmetries are exploited, in most cases the modal approach requires fewer transforms than the direct approach.

5. Numerical implementation

To implement the scheme it is necessary to sample $\bar{\mathcal{M}}(\mathbf{k}_{t1}, \mathbf{k}_{t2}, \omega)$. Consider sampling $\bar{\mathcal{M}}(\mathbf{k}_{t1}, \mathbf{k}_{t2}, \omega)$ over a set of points $\{\mathbf{k}_t^{(i)}\}$ forming a square-grid over part of the \mathbf{k}_t plane. Assume that the grid is centred on the origin, and consists of N points in total, spaced equally in the k_x - and k_y -directions at intervals of $2\pi/L$: Figure 2a. (26) then becomes a set of simultaneous linear equations:

$$\left\{ \sum_{s=1}^N \sum_{u=1}^3 \left(\frac{2\pi}{L} \right)^2 \left[\hat{\mathbf{x}}_q \cdot \bar{\mathcal{M}}(\mathbf{k}_t^{(r)}, \mathbf{k}_t^{(s)}, \omega) \cdot \hat{\mathbf{x}}_u \right] \left[\hat{\mathbf{x}}_u \cdot \mathbf{V}^{(n)}(\mathbf{k}_t^{(s)}, \omega) \right] \right. \\ \left. = \gamma^{(n)} \left[\hat{\mathbf{x}}_q \cdot \mathbf{V}^{(n)}(\mathbf{k}_t^{(r)}, \omega) \right] \right\}, \quad (30)$$

for $q = 1$ to 3 and $r = 1$ to N . $(2\pi/L)^2$ is the area of the plane associated with each sample point, and $\{\hat{\mathbf{x}}_q\}$ is any set of basis vectors spanning three-dimensional space. Let the matrix

representation of (30) be

$$\sum_{j=1}^{3N} M_{ij} V_j^{(n)} = \gamma^{(n)} V_i^{(n)}, \quad (31)$$

then the problem of solving (26) is reduced to finding the eigenvalues, $\gamma^{(n)}$, and normalised eigenvectors, $V^{(n)}$, of the matrix \mathbf{M} . Computationally, we calculate the M_{ij} using (22), solve for the eigenvalues and eigenvectors using a library function, and then extract the modes sampled over the grid. Because of the choice of grid of points, the Fourier transform reduces to a Discrete Fourier Transform (DFT), for which optimised routines can be used. The space-domain response function, sampled over the grid of points shown in Figure 2b, can then be reconstructed from the transformed modes using (27).

When finding the natural-modes numerically, we must sample the \mathbf{k}_t plane sufficiently well to account for all degrees of freedom. It is easy to appreciate that unless we increase the total number of points, N , as we increase the sampling rate in the k -domain, the resolution in the space domain decreases. In fact, to maintain resolution as the k -domain spacing is decreased, N must scale as L^2 . Increasing N , however, comes with the significant numerical overhead of finding the eigenvector decomposition of a large matrix. The problem can be mitigated to some extent by remembering that all the elements of \mathbf{M} in rows or columns where either $\mathbf{k}_{t1} > \omega/c$ or $\mathbf{k}_{t2} > \omega/c$ are zero. It is straightforward to show that these blocks of zeroes do not affect the eigenvector decomposition, and further that for all modes $V^{(n)}(\mathbf{k}_t) = 0$ when $\mathbf{k}_t > \omega/c$. Consequently, it is possible when performing the eigenvector decomposition to consider the reduced matrix \mathbf{M}_s consisting only of pairs of points where $\mathbf{k}_{t1} \leq \omega/c$ and $\mathbf{k}_{t2} \leq \omega/c$. The values outside the domain \mathbf{k}_t can then be filled with zeroes in a later step to increase the resolution in the spatial domain when the mode is Fourier transformed.

A consequence of this result is that the maximum number of modes that can be recovered depends only on the row (or column) length of \mathbf{M}_s , which is equal to three times the number of points in the grid that fall inside $|\mathbf{k}_t| \leq \omega/c$, and is increased by increasing L . For the discretization to be a good approximation to (26) the number of degrees of freedom must, at the very least, exceed the actual number of natural modes of the system. In practice, this number is not known in advance. To ensure all natural modes of the system were accounted for, we iteratively ran the code with increasing values of L for each value of p/λ . In each case, it was assumed L was sufficient when the non-zero eigenvalues stopped increasing in number and converged on final, individual, values.

6. Simulations I

Figure 3 shows the components of $\mathcal{R}(\mathbf{r}_t)$ for $p/\lambda = 0.25, 0.5, 1, 2$ and 4 . The black square in the centre of each plot represents the geometrically re-imaged absorber. For each value of p/λ , the plots have been normalised to the peak value of \mathcal{R}_1 , and \mathcal{R}_1 is plotted against a

single scale spanning 0 to 1 for all p/λ . The plots for \mathcal{R}_2 to \mathcal{R}_4 have been plotted using a common colour scale for any given p/λ , but the scale changes for different values of p/λ . In [11], Chuss et. al. presented the same quantities using a different, less efficient, numerical method, and it is pleasing to see that the results are in exact agreement.

The \mathcal{R}_i characterise the response of the bolometer to spatially-incoherent partially polarized fields. \mathcal{R}_1 represents the responsivity to the Stokes \mathcal{I} parameter. Since the Stokes \mathcal{I} parameter corresponds to intensity, all physically realizable sources will contribute to the output through this term. The map of \mathcal{R}_1 reflects the general imaging behaviour of the bolometer. This basic output is modified depending on the state of polarisation of the source and the values of \mathcal{R}_{2-4} at the source's location. \mathcal{R}_2 shows how the response is modified if the source is a horizontally polarised, \mathcal{R}_3 if it is diagonally polarised, and \mathcal{R}_4 if it is circularly polarised.

When $p/\lambda \gg 1$, \mathcal{R}_1 indicates that the device is largely only responsive to the intensity of the source over the region bounded by the outline of the re-imaged absorber. \mathcal{R}_{1-3} show that the response is slightly polarisation sensitive, reaching 2% of the intensity response at some points. However, the polarisation-sensitive regions appear only near the edges of the image. Once $p/\lambda < 1$ the optical behaviour changes significantly. The bolometer becomes responsive to the intensity of the field over a circular region that is much larger than the geometrical image of the absorber. There is also significant polarisation dependence, which in the case of $p/\lambda = 0.25$ is 10% of the peak intensity response. Notice that the bolometer is insensitive to the \mathcal{V} component for all values of p/λ , which follows from symmetry considerations. Overall, these plots indicate that the behaviour changes from being that of a classical optical detector to that of a few-mode radio antenna as the size of the absorbing region is reduced below a wavelength.

The increase in polarisation response with decrease in p/λ suggests that the state of coherence of the reception pattern increases, and the number of modes decreases. Figures 4(a)-(c) show how the mode coefficients change as p/λ is varied. In (a) and (b), the coefficients have been scaled by $1/(\alpha p^2)$ to remove the dependence on absolute size. In (c) they have been scaled by $1/\sum_n \gamma_n$ to emphasise the relative contribution of each mode to the output. It can be seen in (a) and (b) that the number of optical modes to which the bolometer is sensitive decreases with p/λ . In the limit $p \ll \lambda$, the bolometer is sensitive, effectively, to only three modes: two of which are degenerate (Figure (c)). In (a) and (b) it can also be seen that for $p/\lambda < 1$ the size of the largest coefficients in each spectrum decreases as p/λ decreases. In general it was found that, for an ordering based on the magnitude of the coefficients, the modes of a given order tend to have same spatial form for all values of p/λ . For the modes examined, the non-zero part of the field is always confined to a $\lambda \times \lambda$ region of the source plane centered on the re-imaged pixel. The size of this area relates to the coherence length

enforced on the response function on the sky by propagation.

Figure 5 shows the Stokes response, when $p/\lambda = 0.25$, broken down into the contributions from the three most significant modes. Very similar behaviour is seen for $p/\lambda = 0.5$. It is clear that the polarisation response is dominated by the first two modes. Combining the first- and second-mode contributions gives the petal structure seen in \mathcal{Q} and \mathcal{U} , which is enhanced by the addition of the third mode. These two modes are degenerate and therefore represent orthogonal states of polarisation of the same spatial mode. Figure 4(c) suggests that the behaviour of any electrically small bolometer, $p/\lambda < 1$, can be modelled by a few modes weighted by the appropriate coefficients, and so it is intriguing to consider the forms of these modes.

7. Far-field illumination

Consider the situation where a bolometer is illuminated directly in the far field. This arrangement will allow us to explore the state of coherence of the *angular* reception pattern. The field over the surface of the detector can be written in terms of a superposition of plane waves:

$$\mathbf{E}_{\mathcal{D}}(\mathbf{r}_t, \omega) = \frac{1}{2\pi} \int d^2\mathbf{k}_t \mathbf{W}(\mathbf{k}_t, \omega) \exp(i\mathbf{k}_t \cdot \mathbf{r}_t), \quad (32)$$

where internal scattering has been ignored, and it has been assumed that the reference surface is at $z = 0$. On substituting (32) into (1) and (2), the power absorbed by the bolometer becomes

$$p(\omega) = \int d^2\mathbf{k}_{t1} \int d^2\mathbf{k}_{t2} \bar{\mathcal{G}}^\dagger(\mathbf{k}_{t1}, \mathbf{k}_{t2}, \omega) \cdot \bar{\mathcal{W}}(\mathbf{k}_{t1}, \mathbf{k}_{t2}, \omega), \quad (33)$$

where $\bar{\mathcal{G}}(\mathbf{k}_{t1}, \mathbf{k}_{t2}, \omega)$ is as defined in (10), and $\bar{\mathcal{W}}(\mathbf{k}_{t1}, \mathbf{k}_{t2}, \omega)$ is as defined by

$$\bar{\mathcal{W}}(\mathbf{k}_{t1}, \mathbf{k}_{t2}, \omega) = \langle \mathbf{W}(\mathbf{k}_{t1}, \omega) \mathbf{W}^*(\mathbf{k}_{t2}, \omega) \rangle. \quad (34)$$

The integral is taken over all possible directions of incidence with respect to the front face of the reference plane. It may also be true, however, that the bolometer is sensitive to radiation incident on its reverse face, and the detector response function can be extended easily to include this possibility. We know that the vector \mathbf{k}_t is related to a wave's direction of origin $\hat{\Omega}$ through

$$\mathbf{k}_t = -k(\hat{x}\hat{x} + \hat{y}\hat{y}) \cdot \hat{\Omega} = -k\bar{\mathbf{L}}_t \cdot \hat{\Omega}; \quad (35)$$

in addition,

$$d^2\mathbf{k}_t = -k^2(\hat{z} \cdot \hat{\Omega})d\Omega. \quad (36)$$

(33) can then be written

$$p(\omega) = \int d\Omega_1 \int d\Omega_2 \bar{\mathcal{A}}_e^\dagger(\hat{\Omega}_1, \hat{\Omega}_2, \omega) \cdot \bar{\mathcal{B}}(\hat{\Omega}_1, \hat{\Omega}_2, \omega), \quad (37)$$

where

$$\bar{\mathcal{B}}(\hat{\Omega}_1, \hat{\Omega}_2, \omega) = \frac{k^4 (\hat{\mathbf{z}} \cdot \hat{\Omega}_1) (\hat{\mathbf{z}} \cdot \hat{\Omega}_2)}{2(2\pi)^2 Z_0} \bar{\mathcal{W}}(-k\bar{\mathcal{L}}_t \cdot \hat{\Omega}_1, -k\bar{\mathcal{L}}_t \cdot \hat{\Omega}_2, \omega), \quad (38)$$

and

$$\bar{\mathcal{A}}_e(\hat{\Omega}_1, \hat{\Omega}_2, \omega) = 2(2\pi)^2 Z_0 \bar{\mathcal{G}}(-k\bar{\mathcal{L}}_t \cdot \hat{\Omega}_1, -k\bar{\mathcal{L}}_t \cdot \hat{\Omega}_2, \omega), \quad (39)$$

The factor $2(2\pi)^2 Z_0$ has been introduced because then $\bar{\mathcal{B}}(\hat{\Omega}_1, \hat{\Omega}_2, \omega)$ takes on the form of a brightness tensor, and $\bar{\mathcal{A}}_e(\hat{\Omega}_1, \hat{\Omega}_2, \omega)$ the form of an effective-area tensor. This factor can be justified more rigorously by using Poynting's theorem. When the sky is incoherent and unpolarised, it may be shown, as expected, that

$$\bar{\mathcal{B}}(\hat{\Omega}_1, \hat{\Omega}_2, \omega) = \frac{1}{2} \left(\bar{\mathcal{I}} - \hat{\Omega}_1 \hat{\Omega}_1 \right) B(\hat{\Omega}_1, \omega) \delta(\hat{\Omega}_1 - \hat{\Omega}_2) \quad (40)$$

and then

$$p(\omega) = \frac{1}{2} \int d\Omega \left[\bar{\mathcal{A}}_e^\dagger(\hat{\Omega}, \hat{\Omega}, \omega) \cdot \left(\bar{\mathcal{I}} - \hat{\Omega} \hat{\Omega} \right) \right] B(\hat{\Omega}, \omega), \quad (41)$$

or

$$p(\omega) = \int d\Omega A_e(\hat{\Omega}, \omega) B(\hat{\Omega}, \omega), \quad (42)$$

which is a well-known result in radiometry [14].

Crucially, it is now possible to find the natural optical modes of the detector in the far-field by solving

$$\int d\Omega_2 \bar{\mathcal{A}}_e(\hat{\Omega}_1; \hat{\Omega}_2, \omega) \cdot \mathbf{U}^{(n)}(\hat{\Omega}_2, \omega) = \gamma^{(n)} \mathbf{U}^{(n)}(\hat{\Omega}_1, \omega). \quad (43)$$

Expressing the integral in terms of spherical polar coordinates this expression becomes

$$\int_0^\pi d\theta_2 \int_0^{2\pi} d\phi_2 \sin \theta_2 \bar{\mathcal{A}}_e(\theta_1, \phi_1; \theta_2, \phi_2) \cdot \mathbf{U}^{(n)}(\theta_2, \phi_2) = \gamma^{(n)} \mathbf{U}^{(n)}(\theta_1, \phi_1), \quad (44)$$

where the ω -dependence has been suppressed for brevity. The integrals are taken over the full sky, rather than just the forward hemisphere. In its present form, the equation is not amenable to solution by the numerical, modal method discussed previously. The factor $\sin \theta_2$ means that the kernel is non-symmetric, unlike the underlying function. Instead, consider the change of variable $u = -\cos \theta$. With this substitution, (43) becomes

$$\int_{-1}^{+1} du_2 \int_0^{2\pi} d\phi_2 \bar{\mathcal{A}}_e(\theta(u_1), \phi_1; \theta(u_2), \phi_2) \cdot \mathbf{U}^{(n)}(\theta(u_2), \phi_2) = \lambda^{(n)} \mathbf{U}^{(n)}(\theta(u_1), \phi_1). \quad (45)$$

In this form, the modes, $\mathbf{U}^{(n)}(\theta(u_2), \phi_2)$, and mode-coefficients, $\gamma^{(n)}$, can be found by sampling at regularly spaced intervals in the u - and ϕ -ordinate, and finding the eigenvalues and eigenvectors of the matrix $\Delta u \Delta \phi \bar{\bar{\mathcal{A}}}_e(\theta(u_1), \phi_1; \theta(u_2), \phi_2)$. Some care must be taken with the values of $\Delta \phi$ and Δu . In the case of the ϕ -ordinate, the integral is taken around a closed loop and as a result the $\Delta \phi$ is constant.

8. Simulations II

The above method was used to calculate the natural modes of the angular reception pattern of the bolometer described in Section 4. Substituting $\bar{\bar{\mathcal{G}}}(\mathbf{k}_{t1}, \mathbf{k}_{t2}, \omega)$ for the model pixel into (39), we find the angular response of the model pixel is given by

$$\begin{aligned} \bar{\bar{\mathcal{A}}}_e(\hat{\Omega}_1, \hat{\Omega}_2; \omega) = & 2\alpha p^2 Z_0 \bar{\bar{\mathcal{I}}} \operatorname{sinc} \left[\frac{p}{\lambda} (\hat{\Omega}_1 - \hat{\Omega}_2) \cdot \hat{\mathbf{x}} \right] \\ & \times \operatorname{sinc} \left[\frac{p}{\lambda} (\hat{\Omega}_1 - \hat{\Omega}_2) \cdot \hat{\mathbf{y}} \right], \end{aligned} \quad (46)$$

where we assume the response in the reverse direction is the same as in the forward direction. Figure 6 is the equivalent of 4(c) for the far-field mode coefficients. As in the case of re-imaged pixels, the number of significant modes decreases rapidly as p/λ falls below unity. The number of modes in this limit tends to three, which are degenerate in this case. We also calculated, although they are not shown here, the angular forms of the first four modes when $p/\lambda = 0.25$. The modes closely resemble electric and magnetic dipoles having different orientations. To establish equivalence, we attempted to fit electric- and magnetic-dipole fields to each of the first four modes. The first three modes showed excellent agreement with fields for x -, y - and z -orientated electric dipoles, and the fourth mode to a z -directed magnetic dipole.

9. Dipole representations

At the end of the previous section we observed that when $p/\lambda = 0.25$ the far field behaviour is dominated by a set of dipole-like modes. This suggests that for small p/λ , (46) should be well described by

$$\bar{\bar{\mathcal{A}}}_e(\hat{\Omega}_1, \hat{\Omega}_2, \omega) \approx \sum_m \sum_n A_{mn}(\omega) \mathbf{D}_m(\hat{\Omega}_1) \mathbf{D}_n^*(\hat{\Omega}_2) \quad (47)$$

where $\{\mathbf{D}_n(\hat{\Omega})\}$ is the set of spherical vector harmonics corresponding to electric- and magnetic-dipoles orientated in the x , y and z directions. The matrix elements are given by

$$A_{mn}(\omega) = \int d\Omega_1 \int d\Omega_2 \mathbf{D}_m^*(\hat{\Omega}_1) \cdot \bar{\bar{\mathcal{A}}}_e(\hat{\Omega}_1, \hat{\Omega}_2, \omega) \cdot \mathbf{D}_n(\hat{\Omega}_2). \quad (48)$$

If A_{mn} is diagonal, it does not automatically follow that the optical modes correspond

to dipole fields. A mode could, for example, consist of a dipole field in combination with a higher order spherical harmonic. A measure of how good the approximation is at a particular wavelength can be obtained by calculating the ratio $\sum_n A_{nn} / \sum_m \gamma_m$, where we have, using (46),

$$\sum_m \gamma_m = \int d\Omega \bar{\bar{\mathcal{I}}} \cdot \bar{\bar{\mathcal{A}}}_e(\hat{\Omega}, \hat{\Omega}, \omega) = 16\pi\alpha p^2 Z_0. \quad (49)$$

If the dipoles correspond to the full set of optical modes, then $\sum_n A_{nn} = \sum_m \gamma_m$. Another useful quantity is $A_{nn} / \sum_m \gamma_m$, which gives the relative responsivity of a bolometer in a particular dipole mode.

The challenge is to find the matrix elements $A_{mn}(\omega)$. The reception patterns associated with differently orientated magnetic dipoles are given by

$$\begin{aligned} \mathbf{M}_x(\theta, \phi) &= N \left(\sin \phi \hat{\boldsymbol{\theta}} + \cos \theta \cos \phi \hat{\boldsymbol{\phi}} \right) \\ \mathbf{M}_y(\theta, \phi) &= N \left(-\cos \phi \hat{\boldsymbol{\theta}} + \cos \theta \sin \phi \hat{\boldsymbol{\phi}} \right) \\ \mathbf{M}_z(\theta, \phi) &= N \sin \theta \hat{\boldsymbol{\phi}}, \end{aligned} \quad (50)$$

where $\hat{\boldsymbol{\theta}}$ and $\hat{\boldsymbol{\phi}}$ are unit vectors, and N is the normalisation factor $\sqrt{3/(8\pi)}$. Using the same notation, the fields associated with differently orientated electric dipoles are

$$\begin{aligned} \mathbf{E}_x(\theta, \phi) &= N \left(\cos \theta \cos \phi \hat{\boldsymbol{\theta}} - \sin \phi \hat{\boldsymbol{\phi}} \right) \\ \mathbf{E}_y(\theta, \phi) &= N \left(\cos \theta \sin \phi \hat{\boldsymbol{\theta}} + \cos \phi \hat{\boldsymbol{\phi}} \right) \\ \mathbf{E}_z(\theta, \phi) &= N \sin \theta \hat{\boldsymbol{\theta}}. \end{aligned} \quad (51)$$

When using (50) and (51) in (48) it is beneficial to introduce the operator

$$\begin{aligned} \bar{\bar{\mathcal{T}}} &= \left(\hat{\boldsymbol{\theta}}_1 \hat{\boldsymbol{\theta}}_1 + \hat{\boldsymbol{\phi}}_1 \hat{\boldsymbol{\phi}}_1 \right) \cdot \left(\hat{\boldsymbol{\theta}}_2 \hat{\boldsymbol{\theta}}_2 + \hat{\boldsymbol{\phi}}_2 \hat{\boldsymbol{\phi}}_2 \right) \\ &= [\cos \theta_1 \cos \theta_2 \cos(\phi_1 - \phi_2) + \sin \theta_1 \sin \theta_2] \hat{\boldsymbol{\theta}}_1 \hat{\boldsymbol{\theta}}_2 + \cos \theta_1 \sin(\phi_1 - \phi_2) \hat{\boldsymbol{\theta}}_1 \hat{\boldsymbol{\phi}}_2 \\ &\quad + \cos \theta_2 \sin(\phi_2 - \phi_1) \hat{\boldsymbol{\phi}}_1 \hat{\boldsymbol{\theta}}_2 + \cos(\phi_1 - \phi_2) \hat{\boldsymbol{\phi}}_1 \hat{\boldsymbol{\phi}}_2. \end{aligned} \quad (52)$$

Strictly speaking, each of the brackets in the first line of (52) also contains a term of the form $\hat{\mathbf{r}}\hat{\mathbf{r}}$; however, since neither the magnetic dipole fields or the electric dipole fields have a component in the radial direction this term can be dropped without effect. Replacing the idem factor in (46) with $\bar{\bar{\mathcal{T}}}$ is beneficial because the dipole fields can be represented as two-element vectors. The conversion between $[\hat{\boldsymbol{\theta}}_1, \hat{\boldsymbol{\phi}}_1]$ and $[\hat{\boldsymbol{\theta}}_2, \hat{\boldsymbol{\phi}}_2]$ is then handled in a by $\bar{\bar{\mathcal{T}}}$, which can be represented by a 2×2 matrix.

In spherical coordinates, (48) becomes

$$A_{mn}(\omega) = \int_0^\pi d\theta_1 \int_0^\pi d\theta_2 \int_0^{2\pi} d\phi_1 \int_0^{2\pi} d\phi_2 \sin \theta_1 \sin \theta_2 \mathbf{D}_m^*(\theta_1, \phi_1) \cdot \bar{\bar{\mathbf{A}}}_e(\theta_1, \phi_1; \theta_2, \phi_2; \omega) \cdot \mathbf{D}_n(\theta_2, \phi_2). \quad (53)$$

This expression is difficult to solve analytically, and therefore the integrals were evaluated numerically. To check the software, the limiting case $p \rightarrow 0$ was considered. As $p \rightarrow 0$, from (48) and (46) it can be shown that

$$\frac{A_{mn}(\omega)}{16\pi\alpha p^2 Z_0} \rightarrow \frac{1}{8\pi} \int_0^\pi d\theta_1 \int_0^\pi d\theta_2 \int_0^{2\pi} d\phi_1 \int_0^{2\pi} d\phi_2 \sin \theta_1 \sin \theta_2 \mathbf{D}_m^*(\theta_1, \phi_1) \cdot \mathbf{D}_n(\theta_2, \phi_2). \quad (54)$$

The integrals that arise in this case can be evaluated analytically. It is found that only the diagonal elements associated with the electric dipole modes are non-zero, each being equal to $1/3$. These analytical limits were used to check the software.

10. Simulations III

Figure 7 shows how the diagonal elements, A_{nn} , vary with p/λ . Instead of plotting the A_{nn} directly against p/λ , the scaled values $A_{nn}/16\pi\alpha p^2 Z_0$ are shown. There are two advantages with this normalisation: The first is that the curves become independent of the bolometer's sensitivity α and its absolute size p ; the coefficients of a particular device can be found by reading off the graph and rescaling. The second advantage is that the curves provide a measure of the relative responsivity to each dipole mode. The numerical error in the values is of the order of $\pm 1 \times 10^{-4}$. It can be seen from Figure 7 that the numerical values of A_{nn} in the limit $p/\lambda \rightarrow 0$ are in agreement with the analytic values discussed at the end of the previous section. In addition, the values derived through this method are in agreement with those that were found when carrying out the full simulations in Section 8. For non-zero p/λ , it was found that the off-diagonal elements, A_{mn} , are zero (within numerical error) for all values of $p/\lambda \leq 1.5$. This observation indicates that the reception pattern corresponds, to a good order, to an incoherent superposition of electric and magnetic dipoles. The values shown in Figure 7 are proportional to the responsivity of the detector in each of the dipole fields. It can be seen that the bolometer is equally responsive to power in the x - and y -orientated electric dipole fields, and similarly in the x - and y -orientated magnetic dipole fields. This degeneracy is expected from the symmetry of the absorber. As p/λ falls, the responsivity to the electric dipole fields increases, and tends to a limit at $p/\lambda = 0$. The responsivity to the magnetic dipole fields increases, peaks at $p/\lambda \approx 0.75$, and then decreases to zero, as the area tends to zero. The ratio $\sum_n A_{nn} / \sum_m \gamma_m$ at a particular value of p/λ may be calculated from Figure 7 by summing the contributions from each line. Over the range $0 < p/\lambda < 0.5$, $\sum_n A_{nn} / \sum_m \gamma_m$ is close to unity. In this region, the dipole representation therefore provides

a reasonably complete description of the bolometer's behaviour.

11. Thin resistive films

To this point we have considered *volumetric* absorbers, but the methods described can be extended to thin resistive films. 'Thin' is used here to mean the thickness is very much smaller than the skin depth, so currents are confined to flow in the plane of the film. In operation, an incident field induces a surface current density \mathbf{J}_s on the film. Ohmic heating by these currents then results in the film extracting power from the incident field. If the film has surface resistance R_s , and is square with side length p , the absorbed power is

$$p(\omega) = \frac{1}{2} \int_{-\frac{p}{2}}^{\frac{p}{2}} dx \int_{-\frac{p}{2}}^{\frac{p}{2}} dy R_s |\mathbf{J}_s(x, y)|^2. \quad (55)$$

The surface current density results from the total field, and therefore contains contributions from both the incident field and the field scattered by the currents. Strictly, the scattered field and surface current density are related via the Green's dyadic for the space, so a rigorous calculation of the induced current requires solving an integral equation. However, by assuming the induced surface current is a uniform, infinite, sheet an approximate linear relationship between the two quantities may be found. This approach ignores the effects of the edges of the film and the direction of incidence of the radiation, but is sufficient for a first-order model. It can be shown [15] that the field generated by an infinite sheet current lying in the plane $z = 0$ is

$$\mathbf{E}_s(z) = -\frac{Z_0}{2} \mathbf{J}_s \exp(ik|z|). \quad (56)$$

Taking (56) as the scattered field and using the constitutive equation $Z_s \mathbf{J}_s = \mathbf{E}(z) + \mathbf{E}_s(z)$, we find that the induced current can be written in terms of the incident field $\mathbf{E}(z)$ as

$$\mathbf{J}_s(x, y) = \frac{1}{(R_s + Z_0/2)} (\bar{\bar{\mathcal{I}}} - \hat{\mathbf{z}}\hat{\mathbf{z}}) \cdot \mathbf{E}(x, y). \quad (57)$$

The dyadic operator picks out the component of the incident field tangential to the surface, which is necessary since currents can only flow in the plane of the film. (57) shows that the physical effect of the scattering is to increase the apparent surface impedance of the film. Substituting (57) into (55), we obtain

$$p(\omega) = \frac{1}{2} \frac{R_s}{(R_s + Z_0/2)^2} \int_{-\frac{p}{2}}^{\frac{p}{2}} dx_1 \int_{-\frac{p}{2}}^{\frac{p}{2}} dy_1 \int_{-\frac{p}{2}}^{\frac{p}{2}} dx_2 \int_{-\frac{p}{2}}^{\frac{p}{2}} dy_2 \quad (58)$$

$$\left[(\bar{\bar{\mathcal{I}}} - \hat{\mathbf{z}}\hat{\mathbf{z}}) \cdot (\bar{\bar{\mathcal{I}}} - \hat{\mathbf{z}}\hat{\mathbf{z}}) \delta(x_1 - x_2) \delta(y_1 - y_2) \right]^\dagger \cdot \cdot \mathbf{E}(x_1, y_1) \mathbf{E}^*(x_2, y_2),$$

which, when compared with (2), suggests a planar response function of the form

$$\overline{\overline{\mathcal{D}}}(\mathbf{r}_{t1}; \mathbf{r}_{t2}; \omega) = \begin{cases} \frac{1}{2} \frac{R_s}{(R_s + Z_0/2)^2} \left(\overline{\overline{\mathcal{I}}} - \hat{\mathbf{z}}_1 \hat{\mathbf{z}}_1 \right) \cdot \left(\overline{\overline{\mathcal{I}}} - \hat{\mathbf{z}}_2 \hat{\mathbf{z}}_2 \right) \delta(\mathbf{r}_{t1} - \mathbf{r}_{t2}) & \mathbf{r}_{t1} \text{ and } \mathbf{r}_{t2} \text{ on film} \\ \overline{\overline{0}} & \text{otherwise} \end{cases} \quad (59)$$

With the exception of the idem factor, (59) is identical to (20) with $\alpha = R_s/2(R_s + Z_0/2)^2$, which is the power mismatch factor. This mismatch factor could also have been calculated on the basis of transmission line theory. The dyadic operator in (59) is position independent, and so can be taken out of the integral in (10). The angular response function of the resistive film is therefore simply (46) with the $\overline{\overline{\mathcal{I}}}$ replaced by $\left(\overline{\overline{\mathcal{I}}} - \hat{\mathbf{z}}_1 \hat{\mathbf{z}}_1 \right) \cdot \left(\overline{\overline{\mathcal{I}}} - \hat{\mathbf{z}}_2 \hat{\mathbf{z}}_2 \right)$. In a spherical coordinate system, this dyadic constant becomes

$$\begin{aligned} \left(\overline{\overline{\mathcal{I}}} - \hat{\mathbf{z}}_1 \hat{\mathbf{z}}_1 \right) \cdot \left(\overline{\overline{\mathcal{I}}} - \hat{\mathbf{z}}_2 \hat{\mathbf{z}}_2 \right) &= \cos \theta_1 \cos \theta_2 \cos(\phi_1 - \phi_2) \hat{\boldsymbol{\theta}}_1 \hat{\boldsymbol{\theta}}_2 + \cos \theta_1 \sin(\phi_1 - \phi_2) \hat{\boldsymbol{\theta}}_1 \hat{\boldsymbol{\phi}}_2 \\ &+ \cos \theta_2 \sin(\phi_2 - \phi_1) \hat{\boldsymbol{\phi}}_1 \hat{\boldsymbol{\theta}}_2 + \cos(\phi_1 - \phi_2) \hat{\boldsymbol{\phi}}_1 \hat{\boldsymbol{\phi}}_2, \end{aligned} \quad (60)$$

where, as in (52), we have suppressed the parts involving $\hat{\mathbf{r}}$, as dipole fields have no component in the radial direction. As $\hat{\boldsymbol{\phi}}$ has no component in the $\hat{\mathbf{z}}$ direction, (60) differs from (52) only in the term in $\hat{\boldsymbol{\theta}}_1 \hat{\boldsymbol{\theta}}_2$. Consequently, a simple modification is all that is required in order to model thin-film devices.

12. Simulations IV

Figure 8 shows how the diagonal elements of $A_{mn}/\sum_n \gamma_n$ of the thin-film bolometer vary with p/λ . For the resistive film bolometer $\sum_n \gamma_n = (16\pi p^2 Z_0 R_s)/[3(R_s + Z_0/2)^2]$. The off-diagonal elements have not been shown, as they are all zero within numerical error. Unlike the volumetric bolometer, the thin-film bolometer is unresponsive to power in the x - and y -orientated magnetic dipole fields and the z -orientated electric dipole field for all values of p/λ . This behaviour can be explained by considering the current distributions. The z -orientated electric dipole field couples to a sheet of current in the z -direction, while the x - and y -orientated magnetic dipole fields couple to loops of current in the (x, z) and (y, z) planes. All of these distributions require a current normal to the surface of the film, and therefore cannot be supported. The modes that are supported—the x - and y -orientated electric dipoles and the z -orientated magnetic dipole—couple to currents in the plane of the film. For the modes that are supported, the behaviour with changing p/λ is the same as for the volumetric case. Similarly, $\sum_n A_{nn}/\sum_m \gamma_m$, obtained by summing the lines at a particular value of p/λ , is greater than 0.8 for $p/\lambda < 0.5$. Again this indicates the dipole representation provides a good description of the bolometer's far field optical behaviour for small p/λ .

13. Conclusion

We have considered Withington's [6] and Saklatvala's [7] theoretical model of the optical behaviour of free-space power detectors. In the first part of the paper, we presented an efficient numerical technique for simulating the behaviour of ideal bolometric imaging systems, and demonstrated how the intensity and polarisation response change as the size of the absorbing region is reduced below a wavelength: the reception pattern changes, effectively, from being that of a highly multimode classical optical detector to that of a few-mode radio antenna. The changing form results largely from the limitations imposed by the free-space path between the source and detector, and therefore the observed behaviour should be characteristic of all volumetric absorbers. In the second part of the paper, we extended Withington and Saklatvala's theory, and considered the angular response of naked pixels. It was found, for volumetric absorbers having a side length of less than a wavelength, six modes dominate the intensity and polarisation response: three orthogonal electrical dipoles and three orthogonal magnetic dipoles. As the size of the absorber changes, the relative contributions of the modes change. The scheme can be modified easily to cover thin-film absorbers. In this case, current can only be induced in the plane of the film, and the response of small bolometers is dominated by two electric and one magnetic dipoles. By using a striped, rather than continuous, resistive film, one would expect to be able to reduce the response to a single dipole mode. Not only does this work demonstrate that the optical behaviour of any bolometer can be modelled straightforwardly, it also suggests a particularly simple way of modelling the behaviour of electrically small bolometers. The ability to simulate easily the imaging, polarisation, and straylight characteristics of small pixels will be of considerable value when designing imaging arrays.

References

1. M. Audley, R. Barker, M. Crane, R. Dace, D. Glowacka, D. Goldie, A. Lasenby, H. Stevenson, V. Tsaneva, S. Withington *et al.*, "TES imaging array technology for CLOVER," Proc. SPIE **6275**, 24–32 (2006).
2. J. Ruhl, P. Ade, J. Carlstrom, H. Cho, T. Crawford, M. Dobbs, C. Greer, W. Holzapfel, T. Lanting, A. Lee *et al.*, "The South Pole Telescope," Proc. SPIE **5498**, 11–29 (2004).
3. M. Audley, W. Holland, W. Duncan, D. Atkinson, M. Cliffe, M. Ellis, X. Gao, D. Gostick, T. Hodson, D. Kelly *et al.*, "SCUBA-2: A large-format TES array for submillimetre astronomy," Nuclear Inst. and Methods in Physics Research, A **520**, 479–482 (2004).
4. J. Staguhn, C. Allen, D. Benford, E. Sharp, T. Ames, R. Arendt, D. Chuss, E. Dwek, A. Kovacs, S. Maher *et al.*, "GISMO, a 2 mm Bolometer Camera Optimized for the Study of High Redshift Galaxies," Journal of Low Temperature Physics **151**, 709–714 (2008).

5. S. Dicker, B. Mason, P. Korngut, J. Abrahams, P. Ade, J. Aguirre, T. Ames, D. Benford, T. Chen, J. Chervenak *et al.*, “MUSTANG. First light and current status,” in “Infrared and Millimeter Waves, 2007 and the 2007 15th International Conference on Terahertz Electronics. IRMMW-THz. Joint 32nd International Conference on,” (2007), pp. 331–332.
6. S. Withington and G. Saklatvala, “Characterizing the behaviour of partially coherent detectors through spatio-temporal modes,” *Journal of Optics A* **9**, 626–633 (2007).
7. G. Saklatvala, S. Withington, and M. Hobson, “Coupled-mode theory for infrared and submillimeter wave detectors,” *J. Opt. Soc. Am. A* **24**, 764–775 (2007).
8. S. Withington and C. Thomas, “Optical theory of partially coherent thin-film energy-absorbing structures for power detectors and imaging arrays,” *J. Opt. Soc. Am. A* **26**, 1382–1392 (2009).
9. M. Ney, “Method of moments as applied to electromagnetic problems,” *IEEE Transactions on Microwave Theory and Techniques* **33**, 972–980 (1985).
10. S. Withington, C. Tham, and G. Yassin, “Theoretical analysis of planar bolometric arrays for thz imaging systems,” *Proc. SPIE* **4855**, 49 (2003).
11. D. Chuss, E. Wollack, S. Moseley, S. Withington, and G. Saklatvala, “Diffraction Considerations for Planar Detectors in the Few-Mode Limit,” *Publications of the Astronomical Society of the Pacific* **120**, 430–438 (2008).
12. E. Wolf, “New Theory of Partial Coherence in the Space-Frequency Domain. Part I: Spectra and Cross Spectra of Steady-State Sources,” *J. Opt. Soc. Am.* **72**, 343–351 (1981).
13. L. Mandel and E. Wolf, *Optical Coherence and Quantum Optics* (Cambridge University Press, Cambridge, U.K., 1995).
14. J. Krauss, *Radio Astronomy* (Cygnus-Quasar Books, 1986), 2nd ed.
15. H. Eom, *Electromagnetic wave theory for boundary-value problems: an advanced course on analytical methods* (Springer Verlag, 2004).

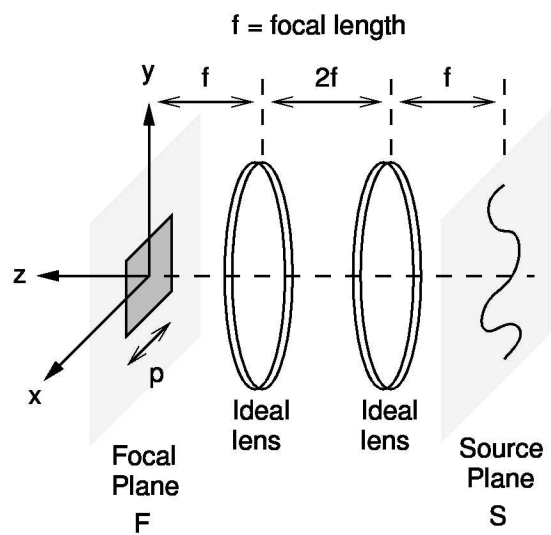


Fig. 1. An ideal imaging system with a free-space bolometer.

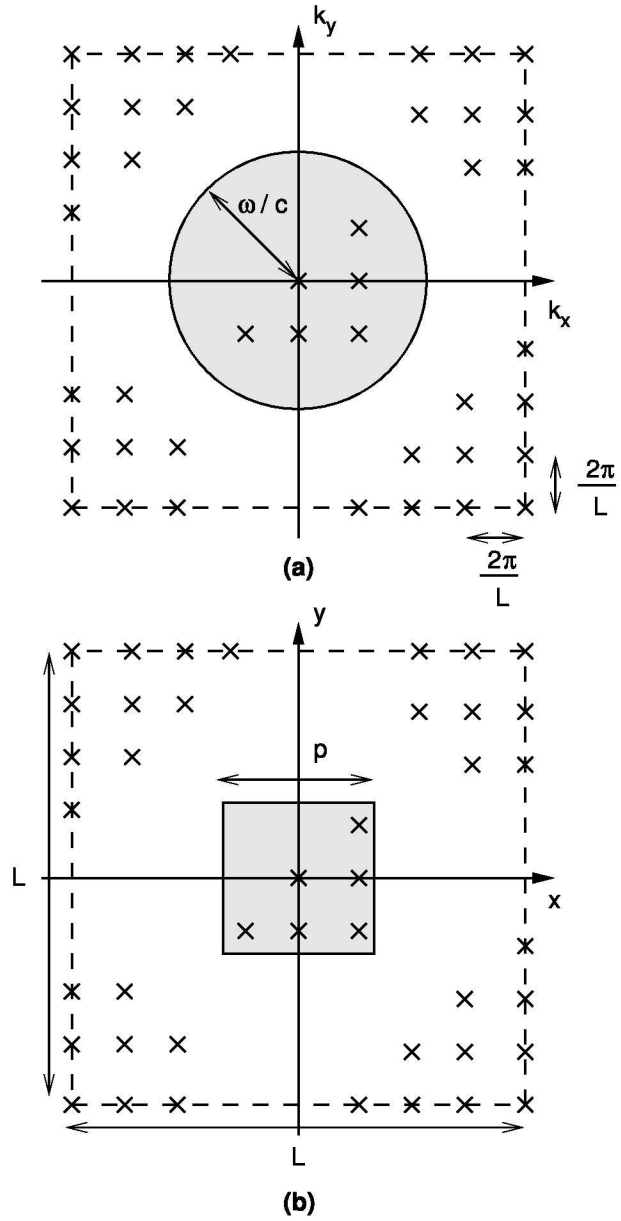


Fig. 2. Figure (a) shows the sampling points in the k -domain, while figure (b) shows the corresponding sampling points in the spatial domain. In each case the total number of points is the same. The grey area in (a) indicates the region of the k -plane where the modes are non-zero.

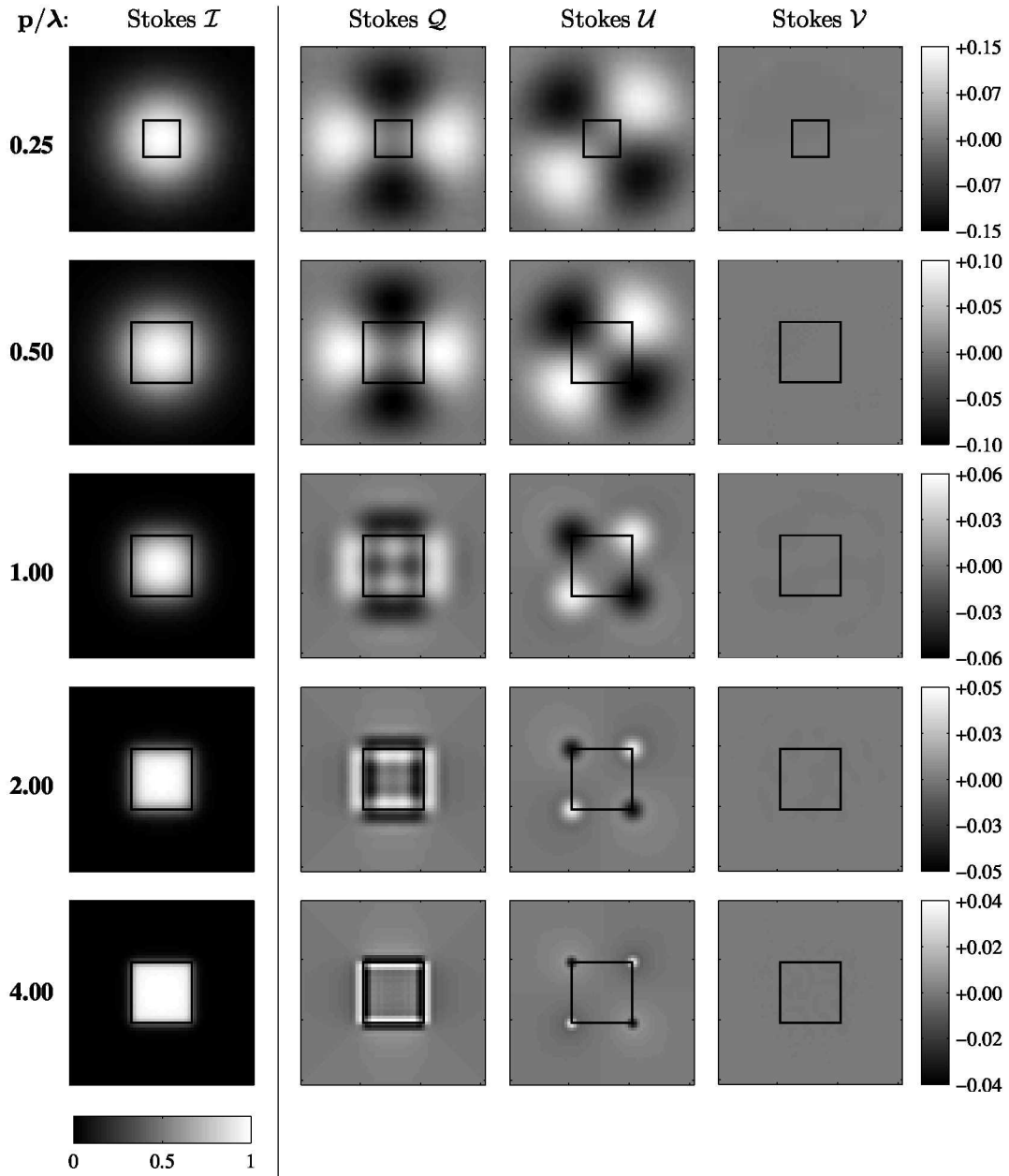


Fig. 3. The Stokes parameters of the optical system shown in Figure 1 for values of p/λ in the range 0.25-4.0. In each plot, the positive x -direction is horizontal from left to right, and the positive y -direction vertical from bottom to top. The small black square is the re-imaged pixel. For each value of p/λ , all four plots are normalised to the peak flux in the corresponding \mathcal{I} plot. Each set of \mathcal{U} , \mathcal{Q} and \mathcal{V} plots use the same colour scale, but the scale's range changes with p/λ .

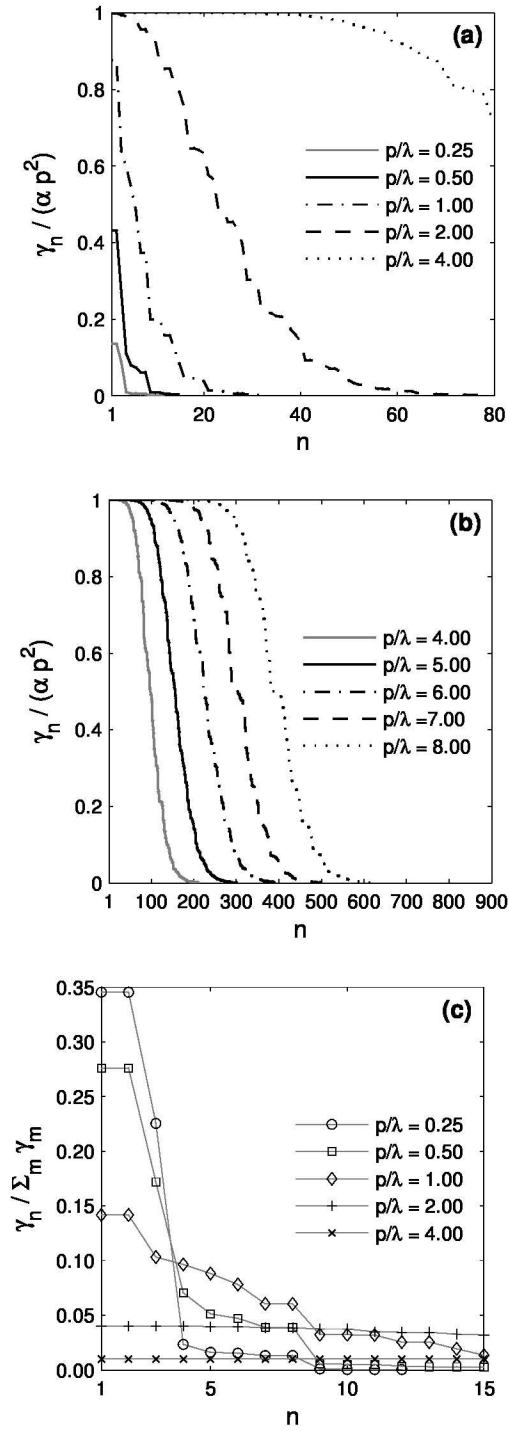


Fig. 4. Spectra of mode coefficients for different values of p/λ . In (a) and (b) the coefficients, γ_n , have been scaled by $1/(\alpha p^2)$; in (c) the coefficients have been scaled by $1/\sum \gamma_n$ to indicate relative contribution.

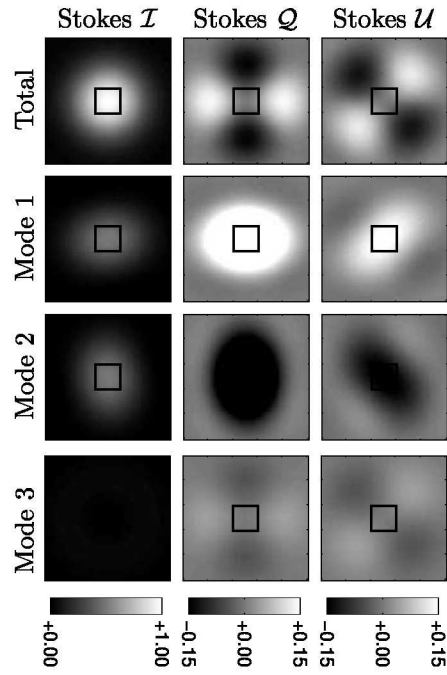


Fig. 5. The contributions from the three coherent-modes with the largest eigenvalues to the Stokes parameters of the reception pattern when $p/\lambda=0.25$. The small black square is the re-imaged pixel. All plots are normalised to the peak flux in the Stokes \mathcal{I} of the full field. The Stokes parameters are plotted against a single colour scale to emphasise their relative contributions.

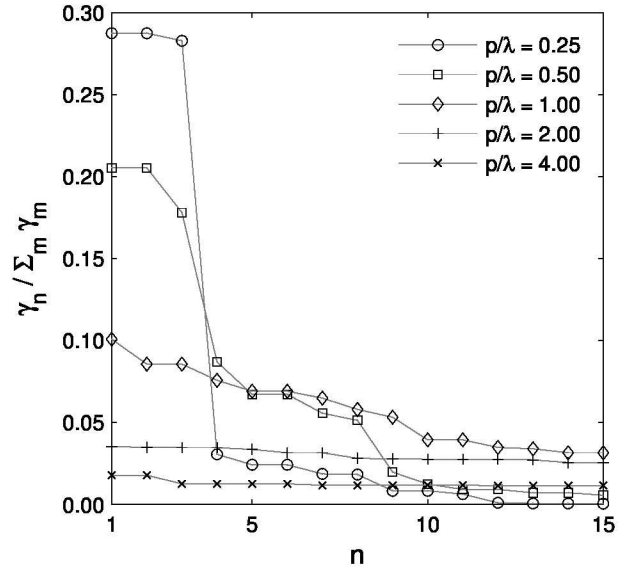


Fig. 6. The normalised coefficients, $\gamma_n / \sum \gamma_m$, of the far-field optical modes.

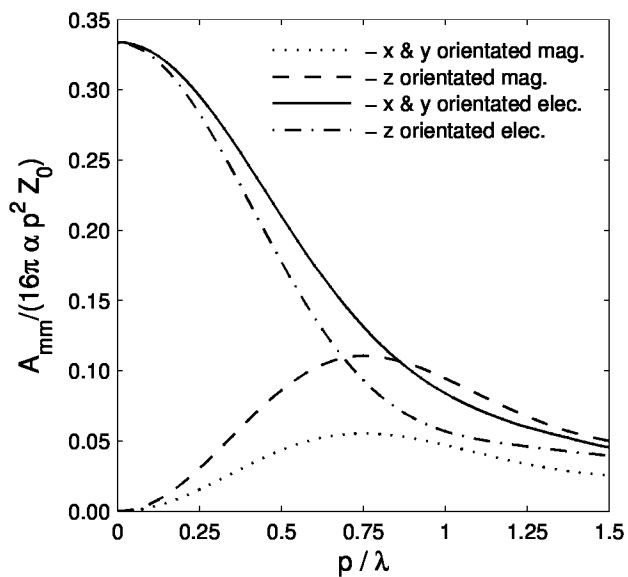


Fig. 7. Diagonal elements of A_{mn} as a function of p/λ for a volumetric absorber. The ratio $\sum_n A_{nn} / \sum_m \gamma_m$ can be calculated for a particular value of p/λ by summing the contributions from each line. This ratio provides a measure of how well the dipole model describes the behaviour of the absorber, and is equal to unity when the description is complete.

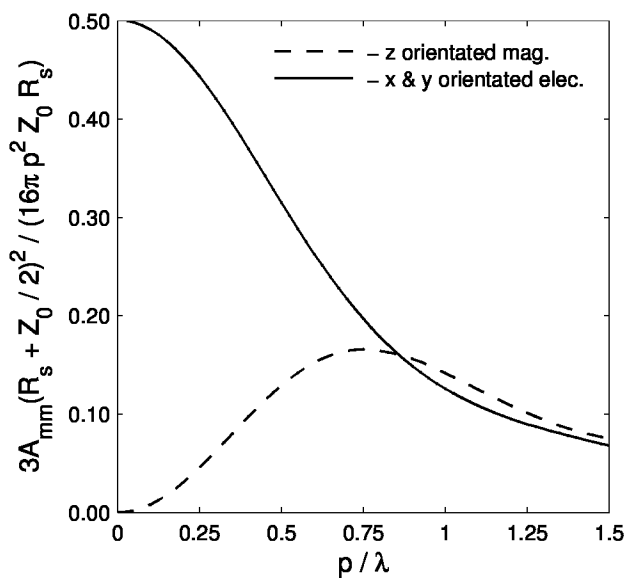


Fig. 8. Diagonal elements of A_{mn} as a function of p/λ for the resistive film absorber